

# Pulsar: A Superconducting Delay-Line Memory

Georgios Tzimpragos<sup>1,+</sup>, Jennifer Volk<sup>2,3,+</sup>, Alex Wynn<sup>3</sup>, Evan Golden<sup>3</sup>, and Timothy Sherwood<sup>1</sup>

<sup>1</sup>UC Santa Barbara, Department of Computer Science, Santa Barbara, CA, 93106, USA

<sup>2</sup>UC Santa Barbara, Department of Electrical and Computer Engineering, Santa Barbara, CA, 93106, USA

<sup>3</sup>Massachusetts Institute of Technology, Lincoln Laboratory, Lexington, MA, 02420, USA

<sup>+</sup>these authors contributed equally to this work

## ABSTRACT

Logic and fabrication advancements have renewed interest in superconductor electronics for energy-efficient computing and quantum control processors. One of the most challenging obstacles ahead is the lack of a scalable superconducting memory technology. Here, we present a superconducting delay line memory based on Passive Transmission Lines built with high kinetic inductors. The developed memory system is fully superconducting; operates at speeds ranging from 20 GHz to 100 GHz with  $\pm 24\%$  and  $\pm 13\%$  bias margins, respectively; and exhibits data densities in the 10s of Mbit/cm<sup>2</sup> with the MIT Lincoln Laboratory SC2 fabrication process. Moreover, its circulating nature allows the miniaturization of control circuitry, the elimination of data splitting and merging, and the inexpensive implementation of both sequential-access and content-addressable memories. Further advancements to high kinetic inductor fabrication processes indicate even greater data densities of 100s of Mbit/cm<sup>2</sup> and beyond.

## Introduction

Superconductor electronics (SCEs) circuits exhibit zero static power dissipation, speed-of-light energy-efficient interconnects, and clock rates in the 100s of GHz<sup>1</sup>. Even more importantly, SCEs can serve as facilitators for integrated classical-quantum computers due to their cryogenic nature and above characteristics<sup>2,3</sup>. Despite advances in fabrication<sup>4</sup>, tools<sup>5,6</sup>, and logic levels<sup>7-9</sup>, however, the lack of a reliable high-speed and high-density superconducting memory impedes the development of practical SCE systems<sup>10</sup>.

Direct application of single flux quantum (SFQ) principles to memory leads to designs with low access latency but insufficient density<sup>11</sup>. Recently-proposed arrays of vortex transition (VT) cells can store up to 1 Mbit of data per square centimeter<sup>12</sup> and are the densest experimentally-verified superconducting memory devices to date. The dimensions of a VT cell—and, in turn, the density of such a memory system—are defined by the length of superconducting flux transformers. Reducing the length of flux transformers while still providing the same inductance, though, is extremely challenging due to spacing requirements. Hybrid architectures that combine SFQ and complementary metal-oxide semiconductor (CMOS) technologies provide better scalability<sup>13</sup>. Nevertheless, CMOS units are slow, usually reside outside of the 4.2 Kelvin cryocooler in which superconducting electronics are placed, and consume a significant amount of power, especially due to their resistive interconnects. A great deal of effort has also been invested in memory cells employing special magnetic materials<sup>14-18</sup>. While promising in many aspects, these approaches suffer from complex device structures, and thus do not scale as desired. Finally, nanowire-based memories provide an interesting alternative<sup>19-21</sup>. In contrast to the attempts discussed above, nanowire-based memories rely on kinetic, rather than geometric, inductance; therefore, they do not have the same miniaturization challenges. Moreover, the use of thermally-coupled cryotrons and row-select heaters eliminates the need for external addressing circuitry in nanowire memories<sup>21</sup>. However, the thermal variation introduced by the heaters causes fluctuation in the kinetic inductance of the hTron-channels, making this likely the reason that arrays of superconducting nanowire memory cells exhibit prohibitively high error rates.

In this paper, we present a superconducting delay line memory based on Passive Transmission Lines (PTLs), which are lengths of superconducting wire that convey single flux quanta. Superconducting PTLs exhibit zero resistive attenuation and are commonly used for signal routing in large-scale SFQ designs because they contain no active elements<sup>22</sup>. If used to form loops, though, they can also be thought of as memory devices. Figure 1 illustrates a PTL loop, where SFQ pulses are introduced at one end of the line, travel along it for a given time, are picked up at the output end, and again transmitted to the input end to repeat the cycle, as shown in Figure 2 (i). Reading and writing is accomplished by interrogating locations (addresses) in a time-serial way. This serialization allows the time sharing of control circuitry and forgoes data splitting and merging, which leads to minimal hardware overhead for addressing. Thus, memory density is primarily defined by the operating speed of the

interface circuitry and the pulse travel speed in the PTL, as will be discussed below in more detail.

Generally speaking, the use of delay lines in memory implementations is not new; in fact, the first delay line memory was acoustic, invented by Eckert and Mauchly in 1947<sup>23</sup>, and published by Auerbach, Eckert, et al. in 1949<sup>24</sup>. In the mid 1950s, IBM produced the 650 calculator that was based on a magnetic delay line memory, known as drum memory<sup>25,26</sup>. Approximately a decade later, Oregon State University designed NEBULA, a medium-speed serial digital computer using a content-addressable memory (CAM) constructed from 35 glass delay lines<sup>27</sup>. A similar idea was also utilized by IBM again in the 1970s for the construction of the non-volatile bubble memory, which stores bits of data in small magnetized areas, known as bubbles, and relies on shifting these bubbles to perform read and write operations<sup>28</sup>. Moreover, racetrack memories, developed more recently, promise to deliver high performance at low cost by storing data in a series of domain walls (DW) along magnetic nanowires. In this case, reading and writing happen by passing a current through the nanowires, which forces DWs to move along them accordingly<sup>29,30</sup>.

When it comes to superconductor electronics, though, the concept of realizing memory through data circulation is nearly unexplored. In the late 1990s, Hattori et al.<sup>31</sup> presented a first attempt to utilize a  $\text{YBa}_2\text{Cu}_3\text{O}_{7-\delta}$  (YBCO) coplanar delay line for the construction of high-speed cell buffer storage for asynchronous transfer mode (ATM) switching systems. Another effort was made in 2016 by Ishida et al.<sup>32</sup>, who proposed an SFQ cache architecture that relies on circular shift registers built from synchronous destructive read-out (DRO) cells. Although these approaches provide evidence of the feasibility and speed of superconducting delay line memories, they fail to achieve high capacities or sufficient addressing capabilities. For example, a CMOS-based  $2 \times 2$  crossbar switch was used to interface to the YBCO coplanar delay line<sup>31</sup>. But this crossbar design cannot operate at more than 10 GHz, latch input data for more than one cycle, or non-destructively read out stored data. Moreover, the pulse travel speed in the YBCO line is  $0.434c$ , where  $c$  is the speed of light, which leads to a minimum spacing of 1.3 cm between two consecutive SFQ pulses, and thus the opportunity for a high-density superconducting memory is wasted. Regarding the DRO-based cache architecture<sup>32</sup>, the use of synchronous cells to form a circular shift register restricts both energy and area efficiency. Furthermore, the decision to perform controlled shifting through a sequence of clock pulses—the length of which is calculated based on the provided address and the register's current position—introduces additional overhead.

In contrast, the design presented here relies solely on existing superconducting cells, operates at speeds of up to 100 GHz, holds input data, non-destructively reads out stored data, and does not require any shift pulses for addressing. Various PTL designs are explored for their area trade-offs, including options from both well-established and more developmental fabrication processes. In this array of choices, the SFQ travel speed in the PTL can be as low as  $0.007c$ , thus giving densities that reach 10s to 100s of  $\text{Mbit/cm}^2$ . More aggressive approaches indicate that memory densities on the order of 1,000s of  $\text{Mbit/cm}^2$  might be possible. Our analysis of DC current bias margins indicates a tolerance to variations ranging from  $\pm 24\%$  at 20 GHz to  $\pm 13\%$  at 100 GHz.

## Results

### Architecture Description and Functional Evaluation

The configuration of the proposed passive superconducting memory system is illustrated in Figure 2 (i). The design consists of a superconducting delay line and a control logic block. The delay line serves as the circulating loop storage and delays any data that arrives at its input (*loop\_data\_in*). The delay introduced by the loop depends on the line's length and the pulse travel speed in the line. At the end of each round trip, the delayed data at the output of the line (*loop\_data\_out*) feeds into the controller, which serves as a memory interface. The controller is responsible for deciding whether signals from the feedback path (*loop\_data\_out*) or the input (*write\_data*) will be forwarded to the delay line (*loop\_data\_in*) for another round, or copied and forwarded to the readout port (*read\_data*).

The block diagram of the controller is provided in Figure 2 (ii). Temporal signals, generated by comparing the value of an address counter with a target address, are used for addressing. The Merger cell, denoted with the letter *m*, stitches together and forwards all signals that appear on its two input lines to its single output line. Thus, when the *write\_addr* signal is low and no pulse appears on the corresponding line in the designated interval, its complementary signal, *write\_addr*, is high and the *loop\_data\_out* signal flows from the DRO2R (DRO with two outputs) on the left into the delay line input (*loop\_data\_in*) uninterrupted. Otherwise, when the *write\_addr* signal is high, the *loop\_data\_out* signal is ignored, the content of the DRO2R is cleared, and *write\_data* is forwarded to the delay line input and readout circuitry. The use of differential signalling for the *write\_address* enables the correction of data timing distortions in both the control circuitry and memory loop. The readout circuitry on the right also consists of a DRO2R cell, which in this case is loaded by the *read\_address* signal. As with the first DRO2R, there are two cases: in the first, the arrival of a pulse on *loop\_data\_in* pushes the stored value to the Q0 output port (*read\_data*); in the second, the complementary *read\_address* signal clears the cell, flushing the stored value.

Simulation results for a superconducting memory system built with this controller and a passive delay line are provided in Figure 3. In the shown examples, three memory addresses are supported, and the memory controller operates at 100 GHz. A high *write\_data* signal is provided before interval 0 of the first rotation, or trip 0, and both the *write\_address* and *read\_address*

lines are asserted in interval 1. Upon the arrival of the *write\_address* signal, a pulse appears on the *loop\_data\_in* line, which demonstrates a successful memory write operation. The appearance of a *read\_data* pulse after the arrival of the *read\_address* signal also indicates that write operations have higher priority than read. To illustrate the non-destructive nature of readout, in the second round trip of Figure 3 (i), *read\_address* is set to 1 again but no *write\_address* is provided this time. A pulse appears on the *read\_data* line, satisfying the specification. In a similar fashion, to demonstrate a successful overwrite, in the second round trip of Figure 3 (ii), *write\_address* is set to 1 but no *write\_data* pulse is given (denoting a logical False). As anticipated, no pulse appears on the *loop\_data\_in* line after this operation.

Note that the presented memory system allows one to search and operate on all of the memory contents while waiting for the entire circulation time to pass, thereby eliminating the need to broadcast to or continuously poll individual cells. The design's rotating nature not only circumvents classic fan-in and fan-out limitations of superconductor electronics, but also supports the addition of multiple write and read ports and the inexpensive implementation of content-addressable memories<sup>27</sup>.

## Circuits Description and Performance Evaluation

To evaluate the performance and feasibility of the proposed architecture, we first provide schematics and simulation results for the memory controller's main components; next, we analyze their latency; lastly, we perform a voltage bias margin analysis for the entire system, including all loading effects due to the control logic, PTL, and accompanying driver and receiver circuitry. The controller, shown in Figure 2 (ii), consists of a destructive readout (DRO) cell, two DRO cells with two output ports each (DRO2R), and a Merger cell. The schematics and corresponding simulations for each cell are provided in Figure 4.

The electrical and timing properties of these cells affect both the performance and functionality of the proposed memory (or any other) system. In particular, electrical issues, typically brought on by parametric variation, can result in under- or over-biased Josephson Junctions (JJs), which in turn can lead to their dysfunction, or delayed or early switching times. To avoid erroneous behavior and ensure correct system timing, the effects of under- and over-biasing are first examined at the cell level. Performing this bias analysis for cells in isolation, however, is not sufficient because it excludes the loading effects that are present in a system setting.

To account for loading, we iteratively measure and tune components to reach the desired timing through an *in-situ* approach—that is, while each cell is fully loaded by the remaining components in the memory controller. The results of this process are shown in Figure 5. Nominal delays are indicated in red. DRO and DRO2R delays are measured as the clock-to-Q delay, while Merger delay is measured as the propagation delay from either input to the output. Delays in each cell increase as bias decreases, and decrease as bias increases. To make bias margins symmetric, we center the nominal delay of each cell between its upper and lower time bounds.

Using interval analysis and the above delays, we estimate the controller's maximum operating frequency, and repeat cell tuning and bias margin measurements. In this case, though, bias margins are measured for the overall system and not each cell. Figure 6 illustrates our results for frequencies ranging from 20 GHz to 100 GHz. We notice that electrical issues drive limitations in bias margin width at lower frequencies, while timing issues are the limiter at higher frequencies. This happens because timing constraints and tolerances get tighter as the address timing interval is reduced. For example, at 100 GHz, the address timing interval is just 10 ps, which leaves little room for the same variations in propagation delay that we observed in Figure 5. Our SPICE simulations show bias margins ranging from  $\pm 24\%$  (at 20 GHz) to  $\pm 13\%$  (at 100 GHz), which are well above the widely accepted  $\pm 10\%$  threshold<sup>33</sup>.

## Data Density Estimation

The physical storage density—that is, bits per area—of a delay-line memory depends on 1) the linewidth and line spacing, set by the the fabrication process; 2) the travel speed, set by the material of choice and the line topology; 3) the relative timing between two adjacent bits, set by the controller's operating frequency; and 4) the number of PTL memory routing layers. We estimate the density of the proposed PTL-based superconducting delay line memory by choosing various settings for each of these free variables and summarize our results in Table 1.

A typical Nb stripline of 250 nm linewidth has a minimum spacing of 250 nm<sup>4</sup> and propagates SFQ pulses at a speed of  $0.3c$ . This leads to data densities of up to  $0.9 \text{ Mbit/cm}^2$  at 100 GHz, if all four metal routing layers are used, and matches the state of the art<sup>12</sup>. Reducing the Nb stripline linewidth and minimum spacing from 250 nm to 120 nm is a possible but more aggressive design choice<sup>34</sup> and results in densities of up to  $1.9 \text{ Mbit/cm}^2$ , exceeding the state of the art by almost  $2\times$ .

By switching device material and topology to a MoN kinetic inductor microstrip with the same dimensions, available on just one layer within MIT Lincoln Laboratory's SFQ5ee<sup>35</sup> or SC2<sup>34</sup> processes, the travel speed of pulses in the line falls by about  $6\times$ . This slowdown yields densities of up to  $1.4$  and  $4.0 \text{ Mbit/cm}^2$  for 250 nm and 120 nm linewidths, respectively, at 100 GHz. Furthermore, scaling the number of layers on which the MoN kinetic inductor is available from one to four—the line topology, in this case, transforms into that of a stripline—increases the data density to  $3.2 \text{ Mbit/cm}^2$  at 20 GHz and  $19 \text{ Mbit/cm}^2$  at 100 GHz for 120 nm linewidth and 120 nm spacing.

At this point, it is evident that the use of materials with increasingly high kinetic inductance is conducive to higher densities. To this end, we explore the potential of NbTiN striplines that exhibit roughly an order of magnitude higher inductance than their MoN counterparts and propagate SFQ pulses at a speed of  $0.011c$ <sup>36</sup>. Our results indicate that for a NbTiN stripline with 100 nm width, 120 nm spacing, four metal routing layers, and controller frequencies between 20 and 100 GHz, the estimated data densities range from 10.7 to 53.3 Mbit/cm<sup>2</sup>.

A more forward-looking approach comes from the use of NbN kinetic inductor nanowires. In the case of an experimentally-tested NbN nanowire with 40 nm linewidth, the inductance scales to 2,050 pH/μm<sup>37</sup>. A roughly proportional drop in capacitance keeps the pulse travel speed the same,  $0.011c$ , but the reduced linewidth pushes the maximum data density to 75.4 Mbit/cm<sup>2</sup> at 100 GHz. A further simulated linewidth reduction to 15 nm causes the inductance to skyrocket to 5,467 pH/μm<sup>37</sup>, which drops the travel speed to  $0.007c$  and increases data density to 140.3 Mbit/cm<sup>2</sup> at 100 GHz. This is equivalent to a pulse spacing of 210 μm along a NbN nanowire, about 60× shorter than that in the YBCO line<sup>31</sup>. Moreover, if CMOS scaling techniques like very large stack-ups—such as the 100-layer stacks used in V-NANDs—were to be adopted in the future by superconducting technology, this NbN nanowire technology could provide a memory density of 3,507 Mbit/cm<sup>2</sup> at 100 GHz operating speed.

## Methods

### Memory Control Circuit Design and Analysis

All simulations were performed in PyLSE<sup>6</sup>, a Python-embedded language for pulse-transfer level design and verification, and WRSPICE<sup>38</sup>, a version of SPICE suited for superconductor-based designs. The JJ model used for WRSPICE simulations is based on MIT Lincoln Laboratory's 100 μA/μm<sup>2</sup> SFQ5ee process parameters<sup>35</sup>. To generate SFQ input pulses in the presence of input DC current stimulation, DC-to-SFQ converters were used.

For the implementation of the controller's main building blocks—shown in Figure 4—publicly available schematics<sup>39,40</sup> served as a starting point. To maximize memory controller's operating frequency and bias margins, the number of JJs on the corresponding circuit's critical path was reduced through customization. In particular, a custom DRO cell with 4 JJs was designed to match the critical currents of the JJs in the surrounding cells, which improved signal fidelity. Moreover, the original DRO2R design consists of symmetrical output paths. However, as can be seen in Figure 2 (ii), only the Q0 output (*data\_out0*) interacts with the delay line loop. Therefore, the internal path from *data\_in* to *data\_out0* was shortened to meet the timing requirements of the loop. Serial inductors in the Merger design were reduced from the original values for the same purpose. Finally, active Splitter cells<sup>39</sup> are traditionally used to provide fan-out for shared nodes; for example, those indicated in Figure 2 by black circles. In this case, a passive splitting technique was used for fan-out, in which JJs surrounding a node with a fan-out of two take on the same sizes as JJs in a Splitter, scaled down by  $\sqrt{2}$ . The combined modifications resulted in a memory controller circuit consisting of 29 JJs and a logic path delay of approximately 10 ps, defined by the sum of DRO2R cell's setup and propagation delays over its bias margins.

Regarding performance evaluation, the timing resolution was set to 0.5 ps, interpolated from the internal step-size that WRSPICE uses, and delays were measured peak-to-peak. More specifically, DRO and DRO2R propagation delays were measured as the clock-to-Q delay, while Merger propagation delay was measured as the propagation delay from either input to the output. Note that delays in each cell tend to increase as bias decreases, and decrease as bias increases. To find the upper and lower time bounds of each cell, detailed bias margin analyses were performed. Particularly, for bias margin measurements, we started from the nominal voltage and decremented by steps of 1% of the nominal voltage over the bias range in which the circuit is operational to get the lower limit, then incremented from nominal to get the upper limit. To ensure that the timing at the limits of the bias margins meet the hold, setup, and propagation time requirements at different target frequencies, static timing analysis using minimum and maximum intervals was performed.

### Memory Density Analysis

Memory density in the PTL delay line is given by

$$Density = \frac{f}{v \times w} \quad (1)$$

where  $f$  is the operating frequency of the memory controller in Hz,  $v$  is the travel speed of single flux quanta in m/s, and  $w$  is the PTL pitch, including linewidth and spacing between lines. Key to improving the memory density is to increase the reciprocal of travel speed times pitch,  $1/(v \times w)$ . In that regard, minimum PTL pitch is determined by the fabrication process. For instance, SFQ5ee<sup>35</sup> allows for the reliable fabrication of Nb and MoN microstrips and striplines with 500 nm pitch. The more advanced SC2<sup>34</sup> process reduces pitch to 240 nm. Further miniaturization is possible with e-beam lithography<sup>37</sup>.

To find the travel speed on PTLs constructed with different materials, the velocity factor equation

$$VF = \frac{c}{\sqrt{L \times C}} \quad (2)$$

was used, where  $c$  is the speed of light in m/s,  $L$  is the inductance per unit length in H/m, and  $C$  is the capacitance per unit length in F/m. The capacitance and inductance values shown in Table 1 were sourced from literature. When geometric inductance is significant, such as in Nb striplines, the inductance scales non-linearly and must be evaluated at each linewidth individually. Based on experimental measurements<sup>34</sup>, a 250 nm-wide Nb stripline has 0.5 pH/μm, while a 120 nm-wide line has 0.65 pH/μm. When kinetic inductance dominates, such as in the cases of MoN and NbTiN striplines and MoN microstrips, inductance does scale linearly and was found by multiplying known inductance per square values—8 pH/□ for MoN striplines and microstrips<sup>41</sup>, and 49 pH/□ for NbTiN striplines<sup>36</sup>—by unit length divided by linewidth. As for their capacitances, we used recently-published fabrication results<sup>34</sup>. For example, a stripline of 120 nm linewidth has a capacitance of 0.19 fF/μm, depending only on the dielectric material and on the geometry. A microstrip of 120 nm linewidth has a capacitance of 0.14 fF/μm.

Regarding 40 nm NbN nanowires, inductance was experimentally found to be 82 pH/□, or 2,050 pH/μm for this width, and capacitance 0.044 fF/μm, owing both to the reduced thickness of the wire as well as the lack of ground planes that sandwich the material<sup>37</sup>. Inductance and capacitance values for 15 nm NbN nanowires were extracted from simulation results<sup>37</sup>. Introducing ground planes above and below these nanowires is expected to increase the capacitance with negligible change to the kinetic-dominated inductance, which would slow the travel speed further—thereby increasing the density.

Finally, another way to increase memory density is to vertically stack PTL layers, in which case the memory density increases by  $N$ —the number of PTL layers.

$$Density = \frac{f}{v \times w} \times N \quad (3)$$

In that regard, Nb striplines with nine planarized superconducting layers, stackable stud vias, self-shunted Nb/AlOx-Al/Nb Josephson junctions, and a single layer of MoN kinetic inductors have been successfully developed<sup>4,42</sup> and allow for four memory layers. To the best of our knowledge, there is no fundamental limitation that constrains vertical growth<sup>39,43–46</sup>.

## References

1. Holmes, D. S., Kadin, A. M. & Johnson, M. W. Superconducting computing in large-scale hybrid systems. *Computer* **48**, 34–42, DOI: [10.1109/MC.2015.375](https://doi.org/10.1109/MC.2015.375) (2015).
2. Li, K., McDermott, R. & Vavilov, M. G. Hardware-efficient qubit control with single-flux-quantum pulse sequences. *Phys. Rev. Appl.* **12**, 014044, DOI: [10.1103/PhysRevApplied.12.014044](https://doi.org/10.1103/PhysRevApplied.12.014044) (2019).
3. Holmes, A. *et al.* NISQ+: Boosting quantum computing power by approximating quantum error correction. In *2020 ACM/IEEE 47th Annual International Symposium on Computer Architecture (ISCA)*, 556–569, DOI: [10.1109/ISCA45697.2020.00053](https://doi.org/10.1109/ISCA45697.2020.00053) (2020).
4. Tolpygo, S. K. *et al.* Developments toward a 250-nm, fully planarized fabrication process with ten superconducting layers and self-shunted Josephson junctions. In *2017 16th International Superconductive Electronics Conference (ISEC)*, 1–3, DOI: [10.1109/ISEC.2017.8314189](https://doi.org/10.1109/ISEC.2017.8314189) (2017).
5. Fourie, C. J. *et al.* ColdFlux superconducting EDA and TCAD tools project: Overview and progress. *IEEE Transactions on Appl. Supercond.* **29**, 1–7, DOI: [10.1109/TASC.2019.2892115](https://doi.org/10.1109/TASC.2019.2892115) (2019).
6. Christensen, M. *et al.* PyLSE: A pulse-transfer level language for superconductor electronics. In *Proceedings of the 43rd ACM SIGPLAN International Conference on Programming Language Design and Implementation*, PLDI 2022 (Association for Computing Machinery, New York, NY, USA, 2022).
7. Tzimpragos, G. *et al.* A computational temporal logic for superconducting accelerators. In *Proceedings of the Twenty-Fifth International Conference on Architectural Support for Programming Languages and Operating Systems*, ASPLOS '20, 435–448, DOI: [10.1145/3373376.3378517](https://doi.org/10.1145/3373376.3378517) (Association for Computing Machinery, New York, NY, USA, 2020).
8. Tzimpragos, G. *et al.* Temporal computing with superconductors. *IEEE Micro* **41**, 71–79, DOI: [10.1109/MM.2021.3066377](https://doi.org/10.1109/MM.2021.3066377) (2021).
9. Tzimpragos, G., Volk, J., Wynn, A., Smith, J. E. & Sherwood, T. Superconducting computing with alternating logic elements. In *2021 ACM/IEEE 48th Annual International Symposium on Computer Architecture (ISCA)*, 651–664, DOI: [10.1109/ISCA52012.2021.00057](https://doi.org/10.1109/ISCA52012.2021.00057) (2021).
10. Holmes, D. S., Ripple, A. L. & Manheimer, M. A. Energy-efficient superconducting computing—power budgets and requirements. *IEEE Transactions on Appl. Supercond.* **23**, 1701610–1701610, DOI: [10.1109/TASC.2013.2244634](https://doi.org/10.1109/TASC.2013.2244634) (2013).
11. Nagasawa, S., Numata, H., Hashimoto, Y. & Tahara, S. High-frequency clock operation of Josephson 256-word/spl times/16-bit RAMs. *IEEE Transactions on Appl. Supercond.* **9**, 3708–3713, DOI: [10.1109/77.783834](https://doi.org/10.1109/77.783834) (1999).

12. Semenov, V. K., Polyakov, Y. A. & Tolpygo, S. K. Very large scale integration of josephson-junction-based superconductor random access memories. *IEEE Transactions on Appl. Supercond.* **29**, 1–9, DOI: [10.1109/TASC.2019.2904971](https://doi.org/10.1109/TASC.2019.2904971) (2019).
13. Van Duzer, T. *et al.* 64-kb hybrid Josephson-CMOS 4 Kelvin RAM with 400 ps access time and 12 mw read power. *IEEE Transactions on Appl. Supercond.* **23**, 1700504–1700504, DOI: [10.1109/TASC.2012.2230294](https://doi.org/10.1109/TASC.2012.2230294) (2013).
14. Feofanov, A. K. *et al.* Implementation of superconductor/ferromagnet/ superconductor  $\pi$ -shifters in superconducting digital and quantum circuits. *Nat. Phys.* **6**, 593–597, DOI: [10.1038/nphys1700](https://doi.org/10.1038/nphys1700) (2010).
15. Vernik, I. V. *et al.* Magnetic Josephson junctions with superconducting interlayer for cryogenic memory. *IEEE Transactions on Appl. Supercond.* **23**, 1701208–1701208, DOI: [10.1109/TASC.2012.2233270](https://doi.org/10.1109/TASC.2012.2233270) (2013).
16. Baek, B., Rippard, W. H., Benz, S. P., Russek, S. E. & Dresselhaus, P. D. Hybrid superconducting-magnetic memory device using competing order parameters. *Nat. Commun.* **5**, DOI: [10.1038/ncomms4888](https://doi.org/10.1038/ncomms4888) (2014).
17. Gingrich, E. C. *et al.* Controllable 0– $\pi$  Josephson junctions containing a ferromagnetic spin valve. *Nat. Phys.* **12**, 564–567, DOI: [10.1038/nphys3681](https://doi.org/10.1038/nphys3681) (2016).
18. Nguyen, M.-H. *et al.* Cryogenic memory architecture integrating spin hall effect based magnetic memory and superconductive cryotron devices. *Sci. Reports* **10**, DOI: [10.1038/s41598-019-57137-9](https://doi.org/10.1038/s41598-019-57137-9).
19. Murphy, A., Averin, D. V. & Bezryadin, A. Nanoscale superconducting memory based on the kinetic inductance of asymmetric nanowire loops. *New J. Phys.* **19**, 063015, DOI: [10.1088/1367-2630/aa7331](https://doi.org/10.1088/1367-2630/aa7331) (2017).
20. Zhao, Q.-Y. *et al.* A compact superconducting nanowire memory element operated by nanowire cryotrons. *Supercond. Sci. Technol.* **31**, 035009, DOI: [10.1088/1361-6668/aaa820](https://doi.org/10.1088/1361-6668/aaa820) (2018).
21. Butters, B. A. *et al.* A scalable superconducting nanowire memory cell and preliminary array test. *Supercond. Sci. Technol.* **34**, 035003, DOI: [10.1088/1361-6668/abd14e](https://doi.org/10.1088/1361-6668/abd14e) (2021).
22. Kameda, Y., Yorozu, S. & Hashimoto, Y. A new design methodology for single-flux-quantum (SFQ) logic circuits using passive-transmission-line (PTL) wiring. *IEEE Transactions on Appl. Supercond.* **17**, 508–511, DOI: [10.1109/TASC.2007.898718](https://doi.org/10.1109/TASC.2007.898718) (2007).
23. Eckert, J. J. P. & Mauchly, J. W. Memory system (1953). US Patent 2,629,827.
24. Auerbach, I., Eckert, J., Shaw, R. & Sheppard, C. Mercury delay line memory using a pulse rate of several megacycles. *Proc. IRE* **37**, 855–861, DOI: [10.1109/JRPROC.1949.229683](https://doi.org/10.1109/JRPROC.1949.229683) (1949).
25. Hamilton, F. E. & Kubie, E. C. The IBM magnetic drum calculator type 650. *J. ACM* **1**, 13–20, DOI: [10.1145/320764.320768](https://doi.org/10.1145/320764.320768) (1954).
26. Frankel, S. Useful applications of a magnetic-drum computer. *Electr. Eng.* **75**, 634–639, DOI: [10.1109/EE.1956.6442018](https://doi.org/10.1109/EE.1956.6442018) (1956).
27. Rux, P. A glass delay line content-addressed memory system. *IEEE Transactions on Comput.* **C-18**, 512–520, DOI: [10.1109/T-C.1969.222703](https://doi.org/10.1109/T-C.1969.222703) (1969).
28. Bonyhard, P. *et al.* Magnetic bubble memory chip design. *IEEE Transactions on Magn.* **9**, 433–436, DOI: [10.1109/TMAG.1973.1067599](https://doi.org/10.1109/TMAG.1973.1067599) (1973).
29. Parkin, S. S. P., Hayashi, M. & Thomas, L. Magnetic domain-wall racetrack memory. *Science* **320**, 190–194, DOI: [10.1126/science.1145799](https://doi.org/10.1126/science.1145799) (2008). <https://science.sciencemag.org/content/320/5873/190.full.pdf>.
30. Parkin, S. & Yang, S.-H. Memory on the racetrack. *Nat. Nanotechnol.* **10**, 195–198, DOI: [10.1038/nnano.2015.41](https://doi.org/10.1038/nnano.2015.41) (2015).
31. Hattori, W., Yoshitake, T. & Tahara, S. A reentrant delay-line memory using a  $\text{YBa}_2\text{Cu}_3\text{O}_{7-\delta}$  coplanar delay-line. *IEEE Transactions on Appl. Supercond.* **9**, 3829–3832, DOI: [10.1109/77.783862](https://doi.org/10.1109/77.783862) (1999).
32. Ishida, K., Tanaka, M., Ono, T. & Inoue, K. Single-flux-quantum cache memory architecture. In *2016 International SoC Design Conference (ISOCC)*, 105–106, DOI: [10.1109/ISOCC.2016.7799755](https://doi.org/10.1109/ISOCC.2016.7799755) (2016).
33. Hashimoto, Y. *et al.* Design and investigation of gate-to-gate passive interconnections for SFQ logic circuits. *IEEE Transactions on Appl. Supercond.* **15**, 3814–3820, DOI: [10.1109/TASC.2005.847487](https://doi.org/10.1109/TASC.2005.847487) (2005).
34. Tolpygo, S. K., Golden, E. B., Weir, T. J. & Bolkhovsky, V. Inductance of superconductor integrated circuit features with sizes down to 120 nm. *Supercond. Sci. Technol.* **34**, 085005, DOI: [10.1088/1361-6668/ac04b9](https://doi.org/10.1088/1361-6668/ac04b9) (2021).
35. Tolpygo, S. K. *et al.* Advanced fabrication processes for superconducting very large-scale integrated circuits. *IEEE Transactions on Appl. Supercond.* **26**, 1–10, DOI: [10.1109/TASC.2016.2519388](https://doi.org/10.1109/TASC.2016.2519388) (2016).

36. Hazard, T. M. *et al.* Nanowire superinductance fluxonium qubit. *Phys. Rev. Lett.* **122**, 010504, DOI: [10.1103/PhysRevLett.122.010504](https://doi.org/10.1103/PhysRevLett.122.010504) (2019).
37. Niepce, D., Burnett, J. & Bylander, J. High kinetic inductance NbN nanowire superconductors. *Phys. Rev. Appl.* **11**, 044014, DOI: [10.1103/PhysRevApplied.11.044014](https://doi.org/10.1103/PhysRevApplied.11.044014) (2019).
38. Incorporated, W. R. WRspice reference manual. Tech. Rep. (2019).
39. Likharev, K. & Semenov, V. RSFQ logic/memory family: a new Josephson-junction technology for sub-terahertz-clock-frequency digital systems. *IEEE Transactions on Appl. Supercond.* **1**, 3–28, DOI: [10.1109/77.80745](https://doi.org/10.1109/77.80745) (1991).
40. Zinoviev, D. *Design and Partial Implementation of RSFQ-based Batcher-Banyan Switch and Support Tools* (Lambert Academic Publishing, New York, 1997).
41. Tolpygo, S. K. *et al.* Superconductor electronics fabrication process with MoNx kinetic inductors and self-shunted Josephson junctions. *IEEE Transactions on Appl. Supercond.* **28**, 1–12, DOI: [10.1109/TASC.2018.2809442](https://doi.org/10.1109/TASC.2018.2809442) (2018).
42. Tolpygo, S. K. *et al.* Deep sub-micron stud-via technology of superconductor VLSI circuits. *Supercond. Sci. Technol.* **27**, 025016, DOI: [10.1088/0953-2048/27/2/025016](https://doi.org/10.1088/0953-2048/27/2/025016) (2014).
43. Radparvar, M. Superconducting niobium and niobium nitride processes for medium-scale integration applications. *Cryogenics* **35**, 535–540 (1995).
44. Villegir, J.-C. *et al.* NbN multilayer technology on R-plane sapphire. *IEEE transactions on applied superconductivity* **11**, 68–71 (2001).
45. Baggetta, E., Ebert, B., Hadacek, N., Villegier, J.-C. & Maignan, M. New design and implementation of a fast modulator in NbN technology. *IEEE transactions on applied superconductivity* **15**, 453–456 (2005).
46. Villegier, J.-C. *et al.* Extraction of material parameters in NbN multilayer technology for RSFQ circuits. *Phys. C: Supercond.* **326**, 133–143 (1999).

## Acknowledgements

The authors would like to thank D. Scott Holmes for his helpful comments and valuable discussions.

## Author contributions statement

G.T. conceived the idea, designed and prototyped the system's microarchitecture, and performed the timing analysis. J.V. designed, simulated, and analyzed the corresponding circuits. G.T., J.V., A.W., and E.G. contributed to the memory density analysis and the writing of the manuscript. T.S. oversaw the project. All authors reviewed the manuscript.

## Corresponding authors

Correspondence to [Georgios Tzimpragos](#) and [Jennifer Volk](#).

## Ethics declarations

### Competing interests

The authors declare no competing interests.

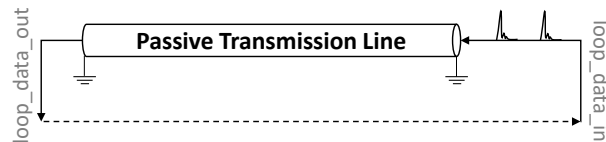


**Figure 1.** Incoming SFQ pulses (*loop\_data\_in*) are introduced at one end of the superconducting passive transmission line (PTL), travel along it at a controlled speed for a given time, are picked up at the output end of the line (*loop\_data\_out*), and again transmitted to the input end for repetition of the cycle.

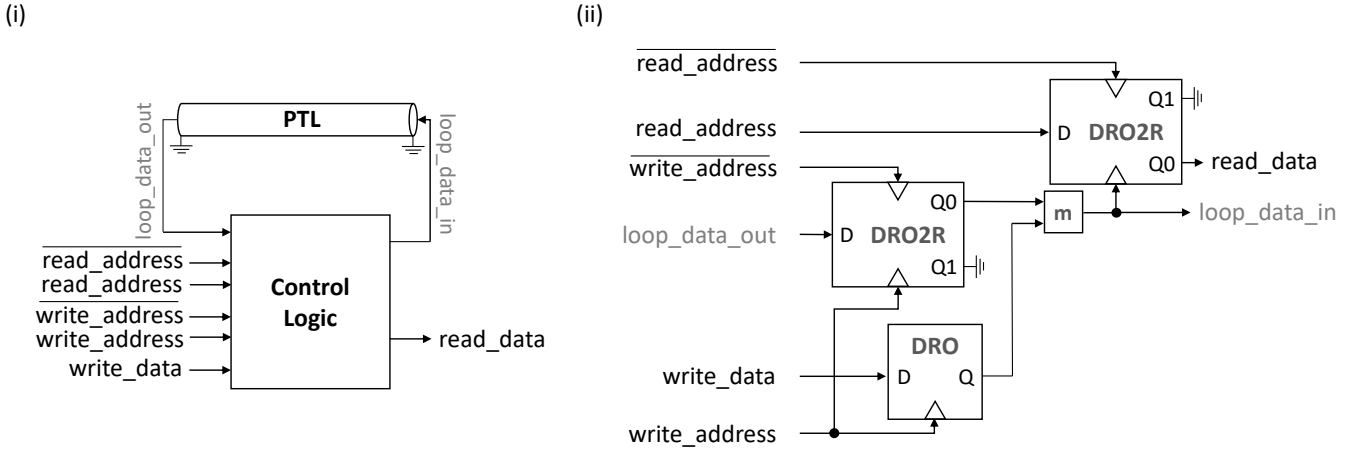


**Figure 2.** Panel (i): Overview of the proposed PTL-based superconducting delay line memory system. Panel (ii): Block diagram of a control logic block enabling sequential-access addressing. A destructive readout (DRO) cell stores a *write\_data* signal until *write\_address* arrives. A DRO cell with two read-out ports (DRO2R) is used to retime and respace the data pulse coming out of the delay line when *write\_address* is low (its complement, *write\_address*, will be high and serve as a synchronizing pulse) or filter it out otherwise. For reading, another DRO2R cell is used. In this case, a high *read\_address* loads this DRO2R cell and a subsequent *loop\_data\_in* or *read\_address* pulse triggers it. If *loop\_data\_in* arrives first, the stored SFQ is forwarded to the *read\_data* line; otherwise, it is sent to the ground. A Merger cell, denoted by *m*, is used to wire two lines together: the first from the output of the DRO for a write operation, and the second from the DRO2R that continues rotating any SFQ that already exist in the loop. A Splitter cell, represented by a black circle, is used for a fan-out of two.

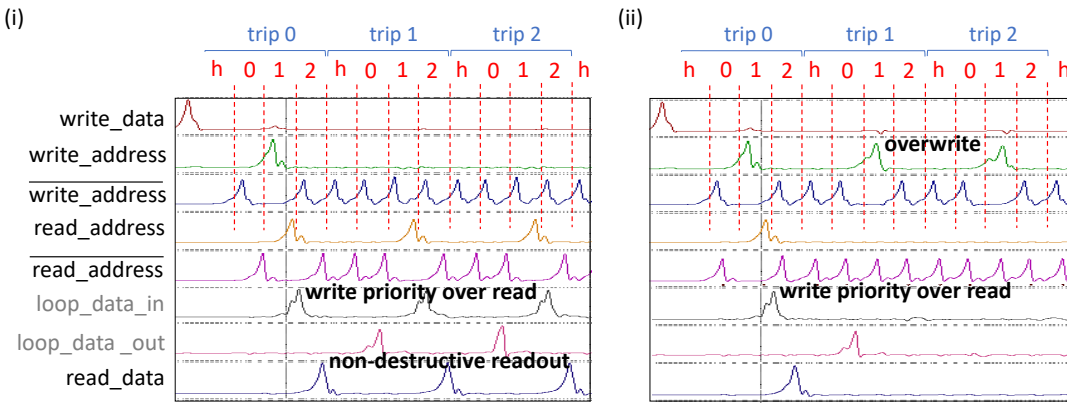


**Figure 3.** WRSPICE<sup>38</sup> simulation results of a passive superconducting memory system using MIT Lincoln Laboratory's 100  $\mu\text{A}/\mu\text{m}^2$  SFQ5ee process parameters and operating at 100 GHz. For simplicity, the number of addresses is set to three. A *write\_data* pulse must always appear before the desired *write\_address*, so each round trip across the recirculating loop storage consists of four cycles, with *h* denoting a header interval. In both shown cases, the loop starts empty and a high *write\_data* signal is provided at the beginning of trip 0. Moreover, in trip 0, both *write\_address* and *read\_address* are set to 1. The appearance of pulses on the *loop\_data\_in* and *read\_data* lines verifies that write has priority over read. In trips 1 and 2 of Panel (i), *read\_address* is set to 1 and no *write\_address* is provided. The appearance of pulses on the *loop\_data\_in* and *read\_data* lines indicates the non-destructive nature of readout. In trips 1 and 2 of Panel (ii), *write\_address* is set to 1, but this time no *write\_data* pulse is given. No pulses appear on the *loop\_data\_in* line, demonstrating a successful overwrite.

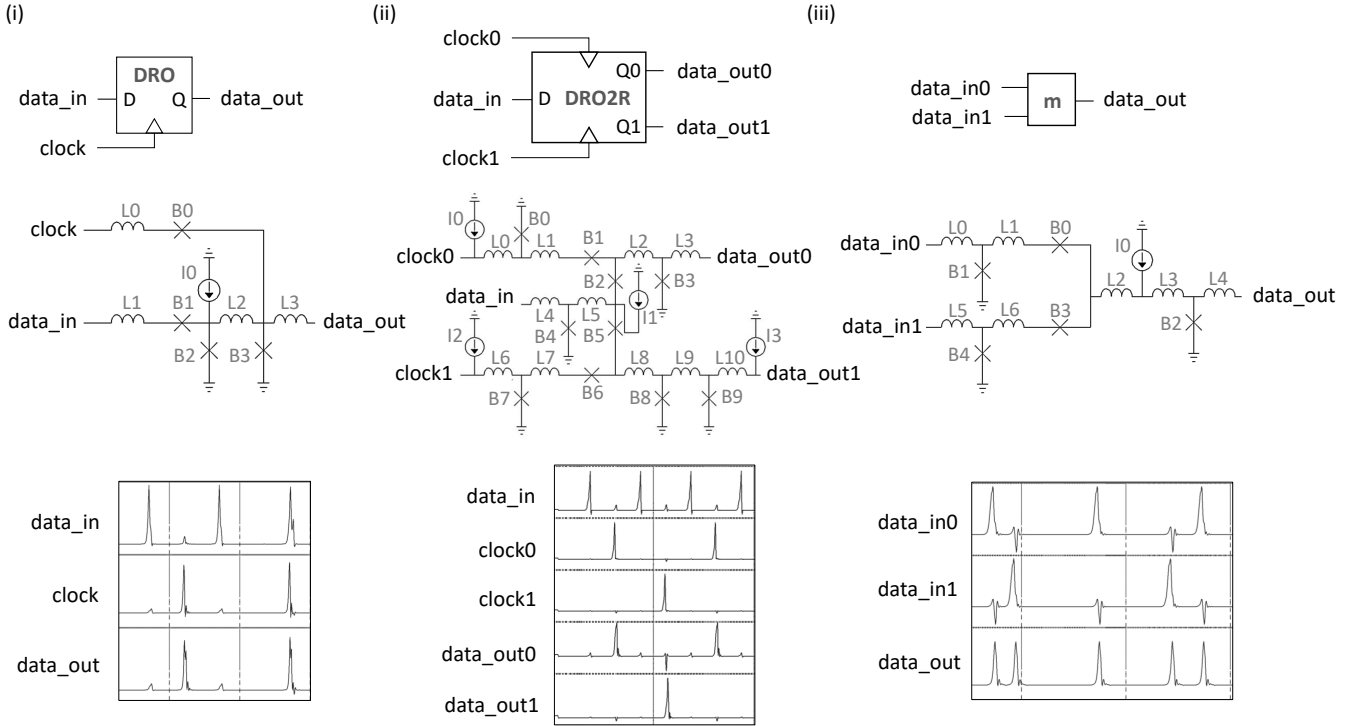


**Figure 4.** Panel (i): symbol, schematic, and simulation results of a destructive readout (DRO) cell. An incoming *data\_in* SFQ pulse is stored in the superconducting quantum interference device (SQUID) formed by B2-L2-B3 until a *clock* pulse arrives. The arrival of a *clock* pulse switches B3 and releases a *data\_out* SFQ pulse. Panel (ii): symbol, schematic, and simulation results of a DRO cell with two readouts ports (DRO2R). The DRO2R cell performs largely the same operation as the DRO—but in this case, the storage element is shared between two parallel loops: B4-L5-B2-L2-B3 and B4-L5-B5-L8-B8 in Figure 4 (ii)<sup>40</sup>. A pulse appearing on either clock input will clear the stored SFQ and push it to the respective output line. Panel (iii): symbol, schematic, and simulation results of a Merger cell. As its name implies, this design passes incoming SFQ pulses on either of its two input ports to its output. To prevent an input SFQ from the opposite line propagating backwards to the input, two blocking Josephson junctions, B0 and B3, are used.

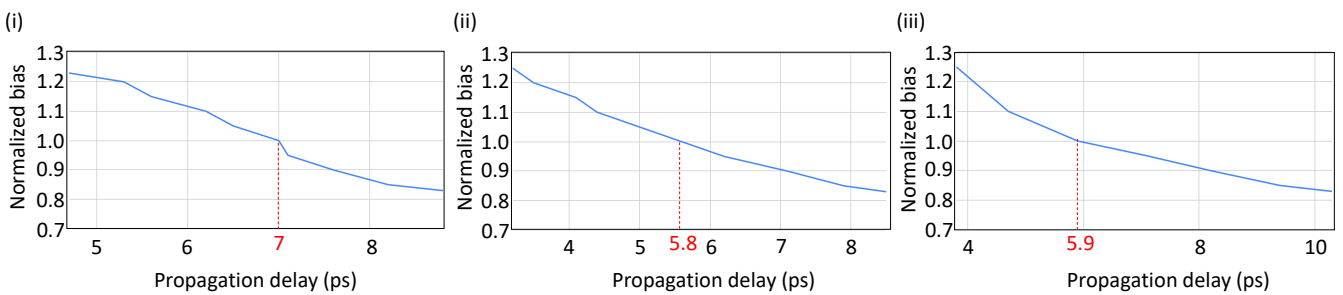


**Figure 5.** Bias versus propagation delay for DRO, DRO2R, and Merger cells. Red markings indicate nominal values. To make bias margins symmetric, we center the nominal delay of each cell between its upper and lower time bounds.

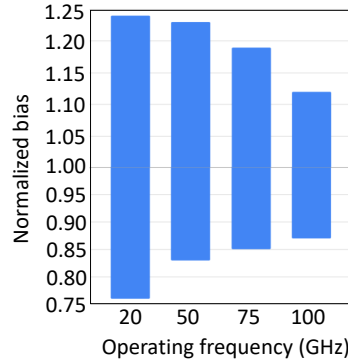


**Figure 6.** Bias margins of the proposed memory system for a variety of operating frequencies.

Device	Linewidth (nm)	Spacing (nm)	Fabrication Process	Memory Layers	Process Maturity	Capacitance (fF/ $\mu$ m)	Inductance (pH/ $\mu$ m)	Travel Speed ( $\times c$ )	Frequency (GHz)	Density (Mbit/cm <sup>2</sup> )								
Nb Stripline	250	250	SFQ5ee	4	Mature	0.25	0.50	0.298	20	0.2								
									50	0.4								
									75	0.7								
									100	0.9								
	120	120	SC2	4	Aggressive	0.19	0.65	0.296	20	0.4								
									50	0.9								
									75	1.4								
									100	1.9								
MoN Kinetic Inductor Microstrip	250	250	SFQ5ee	1	Mature	0.16	32	0.047	20	0.3								
									50	0.7								
									75	1.1								
									100	1.4								
									20	0.8								
	120	120	SC2	1	Aggressive	0.14	66.70	0.034	50	2.0								
									75	3.0								
									100	4.0								
MoN Kinetic Inductor Stripline	120	120	SC2	4	Aggressive	0.19	66.70	0.029	20	3.2								
NbTiN Kinetic Inductor Stripline	100	120	Not Established	4	Academic	0.17	490.5	0.011	50	10.7								
NbN Kinetic Inductor Nanowire	40	120	Not Established	4	Academic	0.04	2,050	0.011	50	26.6								
									75	40.0								
									100	53.3								
									20	15.1								
									50	37.7								
	15	120	Not Established	4	Academic	0.04	5,467	0.007	75	56.6								
									100	75.4								
									20	28.1								
									50	70.1								
									75	105.2								
15									100	140.3								
									20	701.4								
									50	1,753								
									75	2,630								
									100	3,507								

**Table 1.** Memory density estimates for a variety of mature, aggressive, and academic configurations. A mature process is considered one that is well-documented and available as a fabrication option. For example, the MIT Lincoln Laboratory SFQ5ee 100  $\mu$ A/ $\mu$ m<sup>2</sup> process has served as the de-facto standard for fabrication since its introduction in 2016<sup>35</sup>. In a similar fashion, a process is aggressive if it has been evaluated experimentally in real circuits, like the MIT Lincoln Laboratory SC2<sup>34</sup>, but is outside common design rules. The term “academic” is used to indicate that the device has been only theoretically evaluated or experimentally evaluated but not scaled. Capacitance and inductance are also provided because they contribute directly to the SFQ travel speed.